Construction of CuCo₂O₄@CuCo₂O₄ hierarchical nanowire arrays grown on Ni foam for high-performance supercapacitors†

Yan Zhang, Jie Xu,* Yayun Zheng, Yingjiu Zhang,* Xing Hu and Tingting Xu

In this study, hierarchical CuCo₂O₄@CuCo₂O₄ nanowire arrays have been directly fabricated on Ni foam *via* a two-step method that involves hydrothermal and calcination processes. The CuCo₂O₄ nanowires are fully covered by porous CuCo₂O₄ nanosheets. The as-prepared double-metal oxide hierarchical nanowire arrays exhibit superior redox reactivity for supercapacitors. The unique hierarchical nanowire arrays own a specific capacitance of up to 888.9 F g⁻¹ at 2 mA cm⁻², which is much higher than the specific capacitance values of simple CuCo₂O₄ nanowire arrays. The hierarchical CuCo₂O₄ nanostructure shows superior cycling stability, retaining 101.77% of the initial capacitance after 2000 cycles. Moreover, by employing CuCo₂O₄@CuCo₂O₄ as the positive electrode and active carbon (AC) as the negative electrode, an asymmetric supercapacitor (ASC) device was fabricated and it displayed an excellent electrochemical performance. The enhanced electrochemical performance is mainly due to its unique hierarchical structure, which provides good ion and electron transfer, a large number of active sites, and the synergistic effect. In view of their outstanding electrochemical performance and the cost-effective fabrication process, this unique integrated nanoarchitecture may offer great promise as superior electrodes for high-performance supercapacitors.

1. Introduction

With the fossil fuels consumption and worsening environmental pollution problems, sustainable energy storage using clean and renewable energy sources is becoming one of the great challenges in the twenty-first century.[1–4] Compared to the conventional rechargeable devices, such as NiMH batteries and Li-ion batteries, supercapacitor (SC) is considered as a preferable candidate energy storage device due to its high power density, fast charging/discharging rate, long steady cycle life, and being relatively environmentally-friendly.[4–6] In recent years, scientists have made great efforts to study pseudocapacitors because their energy density is substantially higher than that of the electrical double layer capacitors (EDLCs). The performance of pseudocapacitors is largely determined by the faradaic reaction characteristics of the electrode materials,[7,8] and the ternary cobalt-based spinel oxides have been actively pursued because they possess a higher electrical conductivity and better electrochemical performance than those of single cobalt oxides.[9,10]

Among the various ternary cobalt-based spinel oxide electrode materials, spinel copper cobaltite (CuCo₂O₄) has been widely used as a very promising electrode for supercapacitors,[10,11] catalysts,[12] and lithium batteries[13] because it offers many advantages, such as low-cost, availability, and environmental compatibility.[10–13] More significantly, CuCo₂O₄ possesses a greater electrochemical activity and a much better electronic conductivity, at least two orders of magnitude higher than those of the single components of copper oxides and cobalt oxides alone.[10,14] Generally, an ideal supercapacitor should have the merits such as high power density, long cycle life, fast charging/discharging rate, good safety, and low maintenance cost. However, supercapacitors fabricated with one-dimensional (1D) nanomaterials as electrodes have been shown to have difficulties in meeting all these requirements.[8,15–17] Therefore, it is necessary to prepare new nanostructured electrode materials to solve this problem. An efficient way is to synthesize three-dimensional (3D) hierarchical nanomaterials directly on Ni foam as binder- and additive-free electrodes for supercapacitors.[18] The 3D structures and the synergistic effects of component nanomaterials may lead to improved electrochemical performance of the electrodes.[18–20]

To further optimize the electrochemical performance, many hierarchical nanostructure electrode materials have been studied.[21] In a typical hierarchical system, the increasing structural hierarchy could provide better conductivity and increase the active sites of the array structures. Additionally,

School of Physical Engineering, Key Laboratory of Material Physics, Ministry of Education, Zhengzhou University, No. 75, Daxue Road, Zhengzhou 450052, China. E-mail: xujie@zzu.edu.cn; zhangyj2006@zzu.edu.cn

† Electronic supplementary information (ESI) available: The electrochemical characterizations of CuCo₂O₄ and CuCo₂O₄@CuCo₂O₄ electrode; the high magnification SEM image of CuCo₂O₄@CuCo₂O₄ and typical SEM images of CuCo₂O₄ and CuCo₂O₄@CuCo₂O₄ electrode after cycling performance at different magnifications. See DOI: 10.1039/c6ra25970g

a strong synergistic effect could also be realized due to the construction of the hierarchical structure.[22,23] Moreover, the electrode materials would be able to realize a higher electrochemical performance. For instance, Chen *et al.* have reported that $NiCo_2S_4$ nanotube@$NiCo_2S_4$ nanosheet arrays on Ni foam display a superior specific capacity than that of the pure $NiCo_2S_4$ arrays and the hierarchical structure also exhibited an excellent cyclic stability.[24] Zhang *et al.* have reported that $MnCo_2O_2$@-MnO_2 composites exhibit an increased capacitance and better cycling performance as compared to those of the pristine $MnCo_2O_4$ nanowire arrays.[25]

In the present study, hierarchical $CuCo_2O_4$@$CuCo_2O_4$ nanowire arrays were grown on Ni foam as binder- and additive-free electrodes *via* a two-step approach, which involves hydrothermal and calcination processes. Benefiting from the unique properties of the hierarchical nanowire arrays configuration, such as large numbers of active sites, good ion and electron transfer, and good strain accommodation, the as-prepared $CuCo_2O_4$@$CuCo_2O_4$ electrode exhibited a notable electrochemical performance with high capacitance, good rate capabilities, and desirable cycle stability at high current densities.

2. Experimental

The nickel foam was purchased from Suzhou jiashide metal foam Co., Ltd (China) with a 0.1–0.2 mm pore size, 98% porosity, and through-hole rate greater than or equal to 98%. The filter paper was bought from Fushun Dongyang Industry and Trade Co., Ltd (China) of qualitative filter paper with the type of 102. All the reagents used in the experiments were of analytical grade and used as received without further purification.

2.1 Synthesis of the $CuCo_2O_4$ nanowire arrays (NWAs)

In a typical procedure, 1 mmol $Cu(NO_3)_2$, 2 mmol $Co(NO_3)_2$, 12 mmol urea, and 3 mmol CTAB were dissolved in a 70 mL deionized water and stirred to form a clear solution. Fresh Ni foam of a 1×4 cm size was used as the substrate, and it was carefully cleaned with 3 mol L^{-1} HCl solution, deionized water, and ethanol for 20 min each to remove the impurities and oxide layer. The aqueous solution and the Ni foam were transferred to a 100 mL Teflon-lined stainless-steel autoclave, which was sealed, maintained at 120 °C for 12 h, and then naturally cooled down to room temperature. The product was collected and sonicated in deionized water for 10 s, and then washed with deionized water several times. The precursors were dried in a vacuum oven at 60 °C for 3 h and finally annealed in a quartz tube at 300 °C in air for 2 h. The mass loading of $CuCo_2O_4$ NWAs on Ni foam was about 1.1 mg cm^{-2}.

2.2 Preparation of the $CuCo_2O_4$@$CuCo_2O_4$ nanowire arrays (NWAs)

Typically, 1 mmol of $CuCl_2$, 2 mmol $CoCl_2$, 12 mmol urea, and 3 mmol CTAB were dissolved in 70 mL deionized water under stirring. Then, the solution was transferred into a Teflon-lined stainless-steel autoclave. The as-synthesized $CuCo_2O_4$

nanowire array was placed in the autoclave. The autoclave was sealed and heated at 120 °C for 12 h, and then cooled down to room temperature. Subsequently, the substrate was taken out and washed with deionized water several times and dried in vacuum at 60 °C for 3 h. Finally, the precursor was annealed at 300 °C in air for 2 h. After calcination, the average mass loading of the final product was approximately 2 mg cm^{-2}.

2.3 Characterization of the $CuCo_2O_4$@$CuCo_2O_4$ NWAs

The structural characterizations of the synthesized products were performed by X-ray diffraction (XRD, Netherlands Philip X'Pert) using Cu Kα radiation ($\lambda = 0.154056$ nm). The morphologies and microstructures of the as-prepared products were characterized using a scanning electron microscope (SEM, JEOL-JSM-6700F, Japan Electronics), transmission electron microscopy (TEM), and high-resolution transmission electron microscopy (HRTEM) (TEM, JEM-2100, Japan Electronics). The specific surface area and pore size distribution of the materials were determined using the Brunauer–Emmett–Teller (BET) method and Barrett–Joyner–Halenda (BJH) method, respectively (Micromeritics TriStar II 3020 instrument). The mass changes of the products were determined by a microbalance with a readability of 0.1 mg (Mettler, AL204).

2.4 Electrochemical measurements

The electrochemical measurements were carried out using a three-electrode electrochemical cell containing a 2 mol L^{-1} KOH aqueous solution as the electrolyte. The $CuCo_2O_4$ NWAs and $CuCo_2O_4$@$CuCo_2O_4$ NWAs were directly used as the working electrodes, and the area of electrode used in the electrochemical measurement was 1 cm^2. The electrochemical measurements were performed using an electrochemical workstation (CS2350, Wuhan). A standard calomel electrode and Pt foil were used as the reference and counter electrodes, respectively, and all of the experiments were performed at ambient temperature. Electrochemical impedance spectroscopy (EIS) measurements were evaluated using an alternating-current voltage with a 5 mV amplitude in the frequency range from 0.01 Hz to 100 kHz.

For the assembly of the $CuCo_2O_4$@$CuCo_2O_4$//AC device, an AC electrode was prepared by mixing active carbon, acetylene black, and polyvinylidene difluoride at a weight ratio of 85 : 10 : 5, respectively. The slurry was directly coated on a porous nickel foam and dried overnight in a vacuum oven at 60 °C. The ASC device fabricated by separating two electrodes (AC as the negative electrode and $CuCo_2O_4$@$CuCo_2O_4$ as positive electrode) with filter paper was tested in a two-electrode system and using 2 mol L^{-1} KOH as the electrolyte. Based on the three-electrode electrochemical measurement results of both the $CuCo_2O_4$@$CuCo_2O_4$ and AC electrodes, cell balance was achieved by setting the electrode mass ratio of positive/negative to 0.23 (the negative loading mass was around 8.6 mg cm^{-2}). The total mass loading of the active materials was about 10.6 mg.

3. Results and discussion

In this study, the construction of the hierarchical $CuCo_2O_4$@ $CuCo_2O_4$ NWAs for pseudocapacitive electrode was successfully obtained by a facile synthetic strategy including two steps, as schematically illustrated in Fig. 1. Initially, the aligned pristine $CuCo_2O_4$ NWAs were grown on the Ni foam through the hydrothermal and post-annealing processes. Subsequently, a rough porous layer was coated on the surface of $CuCo_2O_4$ NWAs as $CuCo_2O_4$ layers were deposited on the backbone of $CuCo_2O_4$ NWAs through a secondary hydrothermal process, finally resulting in the formation of hierarchical $CuCo_2O_4$@ $CuCo_2O_4$ nanostructures on the conductive substrate as a superior binder- and additive-free electrode.

The XRD patterns of the $CuCo_2O_4$ NWAs and $CuCo_2O_4$@ $CuCo_2O_4$ hierarchical NWAs supported on Ni foam are shown in Fig. 2. The three marked strong peaks are typical peaks of the Ni foam substrate. The diffraction peaks at around $19.07°$, $31.36°$, $36.96°$, $59.59°$, and $65.70°$ can be clearly observed and are well indexed to the (111), (220), (311), (511), and (440) planes of the cubic $CuCo_2O_4$ phase, respectively (JCPDS card no. 01-1155). For the hierarchical nanowire arrays, the pattern shows little difference with that of the bare one. There are no extra peaks in the pattern, demonstrating that the outer layer material was also $CuCo_2O_4$. However, the diffraction peaks of the $CuCo_2$-O_4@$CuCo_2O_4$ hierarchical NWAs are broader than those of the bare one, which may be due to the smaller size of the outer layer $CuCo_2O_4$ crystals or the lower crystallinity.[23]

The morphologies and nanoarchitectures of the $CuCo_2O_4$ NWAs and $CuCo_2O_4$@$CuCo_2O_4$ hierarchical NWAs on Ni foam are shown in Fig. 3. After the hydrothermal and post-annealing processes, large-scale and aligned $CuCo_2O_4$ NWAs uniformly grew on the Ni foam skeletons (Fig. 3a). The needle-structure $CuCo_2O_4$ NWAs appear like numerous "grass", standing on the Ni foam substrate (Fig. 3b). The magnified image shows that $CuCo_2O_4$ NWAs possessed rough surfaces (Fig. 3c). Fig. 3d–f show the typical SEM images of the $CuCo_2O_4$@$CuCo_2O_4$ hierarchical NWAs obtained through the hydrothermal and post-annealing processes with the needle-like $CuCo_2O_4$ NWAs as the substrate. The as-prepared $CuCo_2O_4$@$CuCo_2O_4$ hierarchical NWAs were much denser than the $CuCo_2O_4$ NWAs grown on the substrate (Fig. 3d). Note that the uniformity of the nanoneedle structure was still well retained. The surfaces of the $CuCo_2$-O_4@$CuCo_2O_4$ hierarchical NWAs became rougher (Fig. 3e and
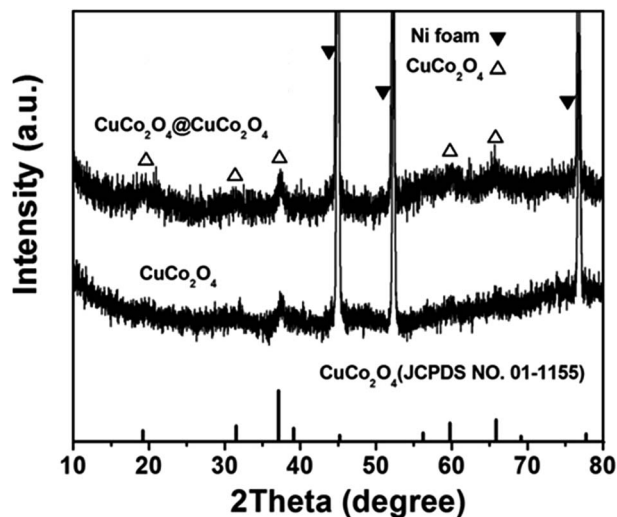

Fig. 2 XRD patterns of the $CuCo_2O_4$ NWAs and $CuCo_2O_4$@$CuCo_2O_4$ NWAs on Ni foam.

f). The diameter of the $CuCo_2O_4$@$CuCo_2O_4$ nanowire was increased, indicating the successful growth of a uniform $CuCo_2O_4$ layer (Fig. 3f and S1†). The inner $CuCo_2O_4$ nanowire and the outer $CuCo_2O_4$ layer have different aspect ratios and dimensions, which may be due to the different substrates used during the reaction process (the $CuCo_2O_4$ nanowire backbone and Ni foam). Obviously, no $CuCo_2O_4$ was packed in the inter-space of the nanowires, suggesting that the $CuCo_2O_4$ layer was preferentially grown on the surface of the inner $CuCo_2O_4$ nanowires. TEM analysis provides the detailed morphology and nanoarchitectures of the as-obtained electrodes. Fig. 3g shows the TEM images of the $CuCo_2O_4$ NWAs and the diameter of the $CuCo_2O_4$ nanowire is about 90 nm at the bottom of the needle-like structure. On closer observation (the inset of Fig. 3g at the upper right), the $CuCo_2O_4$ nanowire shows a mesoporous structure. The measured lattice spacing of 0.24 nm in the HRTEM image of the inset in Fig. 3g at the lower left corresponds to the (311) planes of the cubic $CuCo_2O_4$ nanowire. Afterwards, the needle-like $CuCo_2O_4$ NWAs were employed as the backbone and provide a vast number of sites for the growth of $CuCo_2O_4$ outer layer. The TEM images in Fig. 3f show that the uniform layer of the $CuCo_2O_4$ nanoparticles is covered on the whole surface of the needle-structure $CuCo_2O_4$ nanowires in the
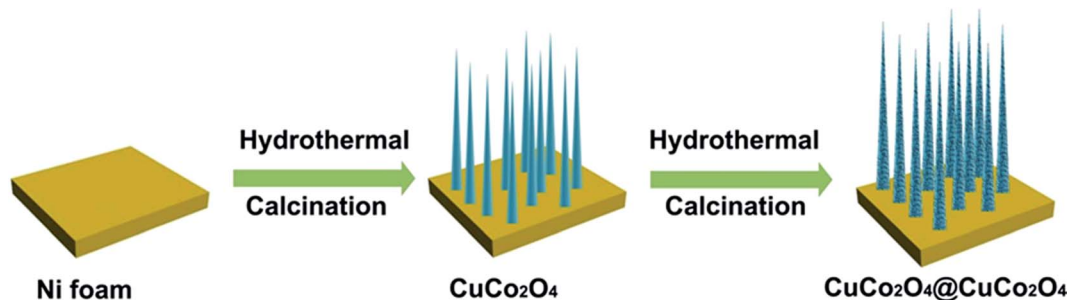

Fig. 1 Schematic for the fabrication process of $CuCo_2O_4$@$CuCo_2O_4$ NWAs on Ni foam.

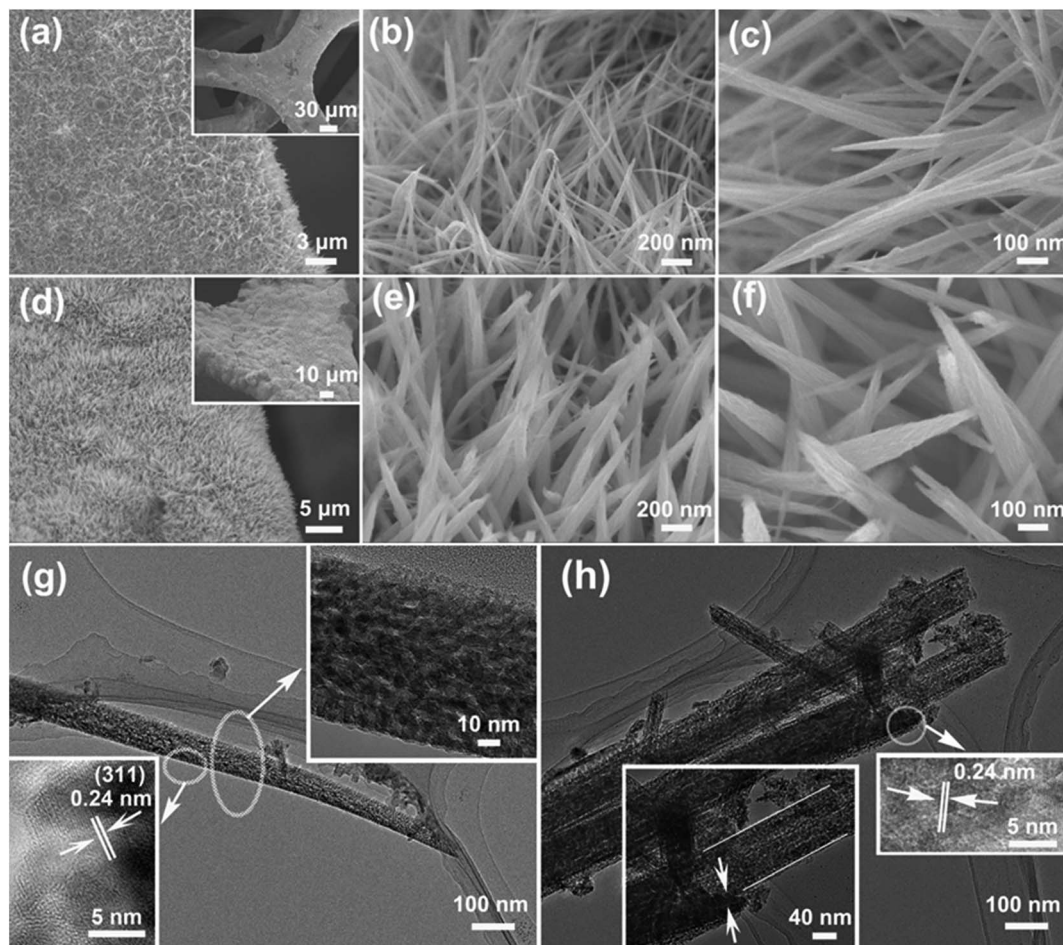**Fig. 3** SEM images of the CuCo$_2$O$_4$ NWAs (a–c) and CuCo$_2$O$_4$@CuCo$_2$O$_4$ NWAs (d–f) on Ni foam at different magnifications. TEM images of the individual CuCo$_2$O$_4$ NWAs (g) and CuCo$_2$O$_4$@CuCo$_2$O$_4$ NWAs (h) and the insets (g and h) are the HRTEM and magnified images.

formation of a hierarchical structure. The magnified image inset in Fig. 3h at the lower left shows that the thickness of the CuCo$_2$O$_4$ nanowires is about 90 nm and that of the CuCo$_2$O$_4$ layer is around 20 nm; the inset at the right shows visible lattice fringes with equal interplanar distance of 0.24 nm, which correspond to the (311) plane of cubic CuCo$_2$O$_4$ and confirms that the outer layer has the same crystal structure as that of the CuCo$_2$O$_4$ nanowires.[24] This unique hierarchical nanoarchitecture has a large number of interspaces, which could improve the utilization rate of the active materials and due to this, the electrolytes are highly accessible to all the electrode materials.[26] The specific surface area and the average pore size of CuCo$_2$O$_4$@CuCo$_2$O$_4$ and CuCo$_2$O$_4$ were 30.95 m^2 g^{-1} and 22.36 m^2 g^{-1}, and 7.5 nm and 8.2 nm, respectively. The CuCo$_2$O$_4$ outer layer with the porous structure was uniformly deposited on the CuCo$_2$O$_4$ nanowire backbone, which could develop the hierarchical structure with an ameliorative pore size distribution as compared to that of the original CuCo$_2$O$_4$ nanowire.

Three-electrode measurements were conducted in 2 mol L^{-1} KOH electrolytes to investigate the electrochemical performance of the electrodes. For comparison, Fig. 4a shows the typical cyclic voltammetry (CV) curves for both the CuCo$_2$O$_4$ and CuCo$_2$O$_4$@CuCo$_2$O$_4$ electrodes within the potential window of

0–0.5 V at the same scan rate of 5 mV s^{-1}. It could be observed that all the CV curves have obvious redox peaks, indicating that the faradic nature of the battery-type electrodes and the redox peaks were mainly governed by the faradaic reactions related to M–O/M–O–OH (M refers to Cu or Co) associated with OH$^-$ anions.[2] Furthermore, the enclosed area of the CV curve for the CuCo$_2$O$_4$@CuCo$_2$O$_4$ hierarchical NWAs electrode was much larger than that for the original CuCo$_2$O$_4$ NWAs electrode, revealing that the hierarchical nanowire arrays have higher electrochemical reaction activity.[27,28] It should be attributed to the following reasons: on one hand, the porous CuCo$_2$O$_4$ outer layer with a huge surface area is beneficial for ion diffusion, intimate electrode/electrolyte contact, and it can provide a large electrochemically active surface area for the redox reactions; on the other hand, it could be because the rational construction of the CuCo$_2$O$_4$@CuCo$_2$O$_4$ hierarchical NWAs can make the best use of each component resulting in a synergistic effect. Note that the redox peak positions of the two electrode materials were obviously different, possibly because the polarization behavior during the CV tests were different in the electrode.[29,30] The polarization behavior is closely associated to the morphology and structure of the electrode material.[30] Therefore, the potential difference for the redox peaks of the two
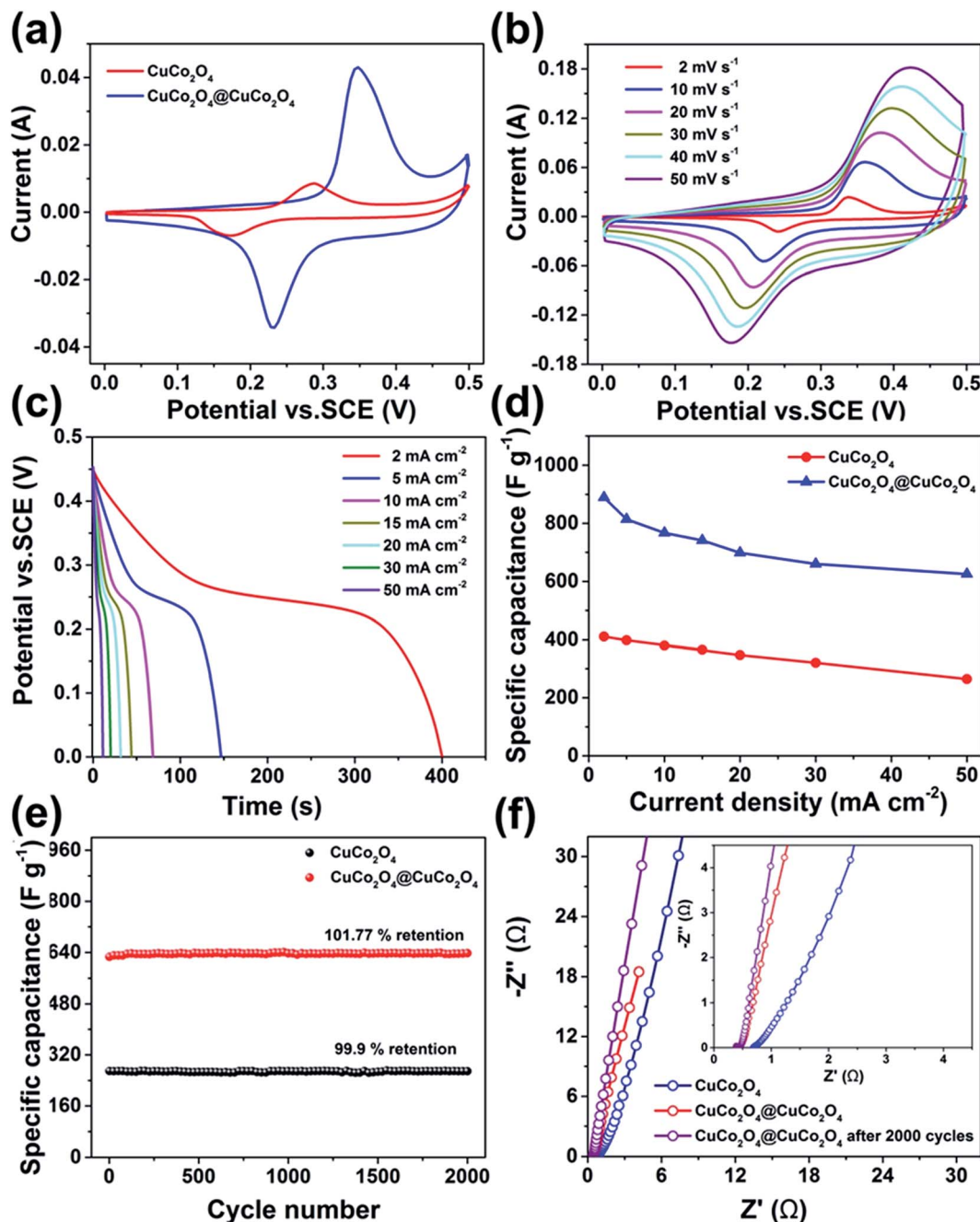
Fig. 4 (a) CV curves of the $CuCo_2O_4$ and $CuCo_2O_4@CuCo_2O_4$ electrodes obtained at a scan rate of 5 mV s^{-1}. (b) CV curves of the $CuCo_2O_4@CuCo_2O_4$ electrode at various scan rates. (c) Charge–discharge curves of the $CuCo_2O_4@CuCo_2O_4$ electrode at different current densities. (d) Specific capacitance of the $CuCo_2O_4$ and $CuCo_2O_4@CuCo_2O_4$ electrodes at different current densities. (e) Long-term cycling stability of the $CuCo_2O_4$ and $CuCo_2O_4@CuCo_2O_4$ electrodes. (f) Impedance Nyquist plots of the $CuCo_2O_4$ electrode and the $CuCo_2O_4@CuCo_2O_4$ electrode before and after 2000 cycles.

electrodes may be attributed to the fact that the $CuCo_2O_4@$ $CuCo_2O_4$ hierarchical nanowire electrode having a porous $CuCo_2O_4$ layer with a larger surface area is beneficial for ion diffusion, intimate electrode/electrolyte contact, and it can provide a large number of electroactive sites for the redox reactions. Moreover, the synergistic effect of the $CuCo_2O_4@$ $CuCo_2O_4$ hierarchical architecture also provided efficient pathways for ion and electron transport. Fig. 4b shows the

typical CV curves of the hierarchical $CuCo_2O_4@CuCo_2O_4$ electrode obtained at the scan rates of 2, 10, 20, 30, 40, and 50 mV s^{-1} in the potential range of 0–0.5 V. As the scan rate increased, the anodic peaks shifted in the anodic direction and the cathodic peaks shifted in the cathodic direction,[31] showing that the faradaic reactions occurred at the interface of the active material and electrolyte.[6,32] Then, the potential difference between the redox peaks (ΔE_p) was generally used to

characterize the reversibility of the faradaic reaction, and a smaller ΔE_p reveals a higher reversibility. The CV curves in Fig. 4b exhibit that the ΔE_p is much higher than the theoretical value of 59.2 mV, illustrating that the electrode was not reversible during the electrochemical process.[6] Moreover, based on Fig. 4b, both cathodic and anodic peak currents (i_p) showed a nearly linear relationship with the square root of the scan rate ($\nu^{1/2}$), which is shown in Fig. S2,† revealing that the electrode reaction corresponds to the quasi-reversible and diffusion-controlled process with the electrolyte involved.[6] The CV curves of the $CuCo_2O_4$ electrode at different scan rates are shown in Fig. S3a.†

Galvanostatic charge–discharge (GCD) measurements were conducted in the potential range from 0 to 0.45 V with various current densities ranging from 2 to 50 mA cm^{-2}. Fig. 4c and S1b† exhibited the GCD curves of the $CuCo_2O_4@CuCo_2O_4$ and $CuCo_2O_4$ electrodes, respectively. The specific capacitance C_s (F g^{-1}) can be calculated from the GCD curves by the equation $C_s = I\Delta t/(m\Delta V)$, where I (A) is the discharge current, Δt (s) is the discharge time, m (g) represents the mass of the electroactive materials, and ΔV (V) is the discharge potential range. According to the equation, the specific capacitances of the electrodes were calculated from the discharge curves and the corresponding results are plotted in Fig. 4d. Impressively, the $CuCo_2O_4@CuCo_2O_4$ electrode delivered high specific capacitances of 888.9, 814.1, 767.1, 741.4, 698.2, 660.0, and 625.4 F g^{-1} at the current densities of 2, 5, 10, 15, 20, 30, and 50 mA cm^{-2}, respectively (Fig. 4d). It can be seen that even by a 25-fold increase in the scan rate, the capacitance retention of the $CuCo_2O_4@CuCo_2O_4$ electrode was about 70.3% of its initial capacitance value. This good rate capability is ascribed to the highly porous structure of the $CuCo_2O_4@CuCo_2O_4$ electrode. The specific capacitance of the $CuCo_2O_4@CuCo_2O_4$ NWAs electrode still retained a value of 625.4 F g^{-1} at 50 mA cm^{-2}. This is because of the diffusion effect of the proton within the electrode, where the inner active sites cannot completely precede the redox transitions at higher current densities.[25] Moreover, the hierarchical nanowire arrays electrode delivered a specific capacitance of 888.9 F g^{-1} at the current density of 2 mA cm^{-2}, which is much higher than that of the pristine $CuCo_2O_4$ NWAs electrode (about 411.4 F g^{-1}).

The long-life cycling performance plays a key role for supercapacitor applications. The long-term cycling stabilities of the $CuCo_2O_4$ and $CuCo_2O_4@CuCo_2O_4$ electrodes were investigated by repeating the GCD tests at 50 mA cm^{-2} for 2000 cycles, as shown in Fig. 4e. For comparison, the original $CuCo_2O_4$ electrode displayed a specific capacitance of 269.3 F g^{-1} (~99.9% capacitance retention). Impressively, even at a very high discharge current density, the $CuCo_2O_4@CuCo_2O_4$ hierarchical electrode still exhibited a high specific capacitance of 626.5 F g^{-1} (~101.77% capacitance retention) after 2000 cycles. The coulombic efficiency during the 2000 charge/discharge cycles was more than 101%, which revealed the electrochemical suitability of the hierarchical $CuCo_2O_4@CuCo_2O_4$ electrode, whose redox reactions were quite feasible. As expected, the $CuCo_2O_4@CuCo_2O_4$ electrode showed high specific capacity, good rate capability, and cycling stability, which can

be mainly due to their multiple merits: first, the direct growth of the $CuCo_2O_4@CuCo_2O_4$ NWAs on the current collector ensures good mechanical adhesion and a fast charge transfer pathway between the active material and current collector; second, the $CuCo_2O_4$ nanowires that were directly grown on the Ni foam allow for good electron transport, and the porous $CuCo_2O_4$ outer layer with a large surface area is beneficial for fast ion diffusion, intimate electrode/electrolyte contact, and it can provide a large number of electroactive sites for the redox reactions; and third, the entire electrode architecture provided efficient pathways for ion and electron transport. Note that the cycling stability of the hierarchical structured $CuCo_2O_4@CuCo_2O_4$ electrode was better than that of the other reported electrodes, such as $ZnCo_2O_4@Ni_xCo_{2x}(OH)_{6x}$ NWAs on Ni foam (81.4% capacitance retention after 2000 cycles at 20 mA cm^{-2}),[33] $NiMoO_4@Ni(OH)_2$ core/shell nanorods on Ni foam (72% capacitance retention after 2000 cycles at 8 mA cm^{-2}),[34] $Co_3O_4@Ni(OH)_2$ NWAs on Ni foam (81.1% capacitance retention after 1500 cycles at 10 A g^{-1}).[35] In addition, EIS measurement was further performed to explain the excellent electrochemical behaviour of the $CuCo_2O_4@CuCo_2O_4$ electrode. Fig. 4f shows the impedance Nyquist plots of the $CuCo_2O_4$ electrode and the $CuCo_2O_4@CuCo_2O_4$ electrode before and after 2000 cycles. In the low-frequency region, the $CuCo_2O_4@CuCo_2O_4$ electrode has a more ideal straight line, revealing that they have a lower diffusion resistance. This can be due to the porous $CuCo_2O_4$ outer layer with a large surface area that has increased the active material utilization and thus facilitated the supply of OH$^-$ to the inner $CuCo_2O_4$ nanowires.[36,37] Obviously, the $CuCo_2O_4@CuCo_2O_4$ electrode also displayed a low bulk resistance and charge-transfer resistance and exhibited high electrochemical activity for the $CuCo_2O_4@CuCo_2O_4$ hierarchical electrode for supercapacitors. This may be because the synergistic effects of the hierarchical architecture of the $CuCo_2O_4@CuCo_2O_4$ nanowires arrays electrode, which can increase the conductivity and improve the ion transfer during the charge/discharge process as compared to those of the bare $CuCo_2O_4$ nanowires arrays electrode.[38] After 2000 cycles, the impedance spectra in a low-frequency region of the $CuCo_2O_4@CuCo_2O_4$ electrode almost remained unchanged. However, in the low-frequency region, the $CuCo_2O_4@CuCo_2O_4$ electrode after 2000 cycles had a more ideal straight line (compared with the $CuCo_2O_4@CuCo_2O_4$ electrode before 2000 cycles), representing more efficient electrolyte and proton diffusion after cycling. This may be because of the full activation of the electrode. The SEM images of the $CuCo_2O_4$ and $CuCo_2O_4@CuCo_2O_4$ electrodes after 2000 cycles at different magnifications are shown in Fig. S4 and S5.† According to the SEM images, it can be observed that the nanowire arrays almost had no change after 2000 cycles, the overall morphology of the product was maintained and the 3D nanowire arrays were still found to densely cover the Ni surface of Ni foam substrate. Therefore, using $CuCo_2O_4$ to design the hierarchical arrays can reach excellent cycling stability.

Furthermore, to evaluate the $CuCo_2O_4@CuCo_2O_4$ hierarchical electrode for practical applications, an asymmetric supercapacitor cell was assembled using AC as the negative electrode and $CuCo_2O_4@CuCo_2O_4$ as the positive electrode.

This configuration benefits from a high energy redox-based ($CuCo_2O_4@CuCo_2O_4$) and a high power EDLC-based (AC) electrode, ensuring high performance of the final device. Fig. 5a shows the individual CV curves of the positive and negative electrodes at a scan rate of 20 mV s^{-1}, obtained separately in a three-electrode configuration. In the case of the AC electrode, the CV curve is almost rectangular in the potential window of −1.0–0 V, revealing the EDLC charge storage mechanism of the carbon-based electrodes. Unlike the AC electrode, the $CuCo_2O_4@CuCo_2O_4$ product had a distorted shape, which showed

clear redox peaks in the voltage range of 0–0.5 V, demonstrating the faradaic nature of the charge storage mechanism. Therefore, the total cell voltage of the ASC device could be as large as 1.5 V, which is based on the working potential windows of the negative and positive electrodes. This operation voltage window value is higher than the thermodynamic decomposition voltage limit of water in aqueous solutions (e.g. >1.2 V) and AC-based symmetric supercapacitor devices (0.8–1.0 V).[39,40] Fig. 5b shows the CV curves of the $CuCo_2O_4@CuCo_2O_4$//AC supercapacitor at different scan rates, illustrating the contribution of

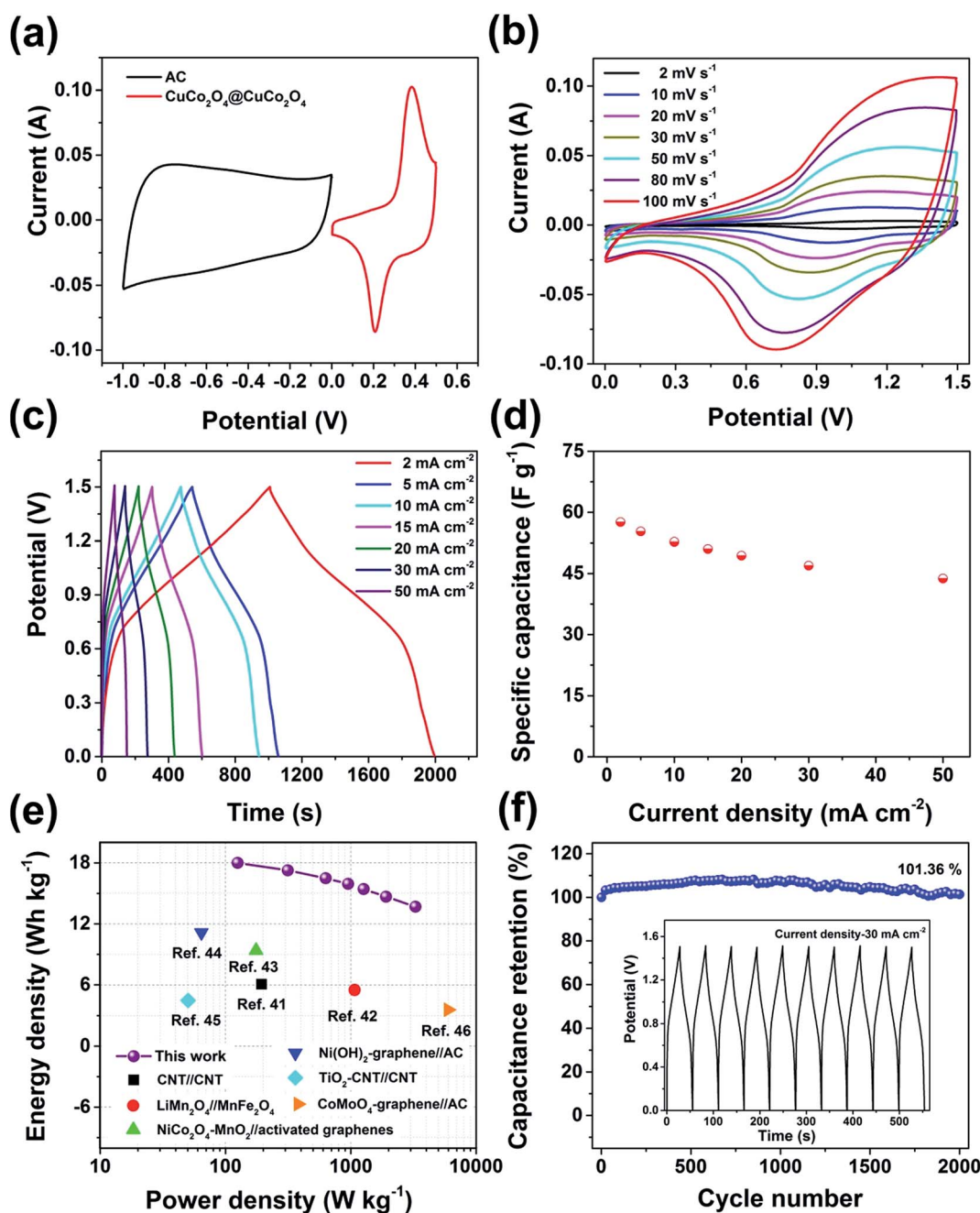Fig. 5 Electrochemical performance of the $CuCo_2O_4@CuCo_2O_4$//AC asymmetric supercapacitor. (a) CV curves of the $CuCo_2O_4@CuCo_2O_4$ NWAs and AC electrodes at a scan rate of 20 mV s^{-1}; (b) CV curves at different scan rates; (c) galvanostatic charge−discharge curves at different current densities; (d) specific capacitance of the device as a function of current density; (e) Ragone plots (energy density vs. power density); (f) cycling performance, inset shows the first 10 cycles of the charge−discharge tests.

both EDLC (0–1 V) and faradaic redox (1–1.5 V) charge storage mechanism. With the increasing scan rates, the CV curves showed no obvious distortion and also showed the fast charge–discharge reversibility of the device. The charge–discharge profiles of the $CuCo_2O_4@CuCo_2O_4//AC$ asymmetric supercapacitor were also evaluated for the applied current densities ranging from 2 to 50 mA cm^{-2}, as shown in Fig. 5c. The specific capacitances of the device calculated from the galvanostatic discharge curves were 57.60, 55.27, 52.76, 51.01, 49.39, 46.93, and 43.78 F g^{-1} at 2, 5, 10, 15, 20, 30, and 50 mA cm^{-2}, respectively (Fig. 5d). Note that the $CuCo_2O_4@CuCo_2O_4//AC$ supercapacitor exhibited excellent rate capability with a high retention rate of 76.0%, even when operated under a high current density of 50 mA cm^{-2}, indicating the good rate performance of the ASC device used in this study.

According to the specific capacitance of the asymmetric supercapacitors, the energy density (E, in W h kg^{-1}) and power density (P, in W kg^{-1}) could be further calculated using the equations $E = 1/2CU^2$ and $P = E/t$, respectively. With the current density increasing from 2 to 50 mA cm^{-2}, the Ragone plot of the estimated energy densities and power densities for the ASC device are shown in Fig. 5e, which displays a high energy density of 18.0 W h kg^{-1} at a power density of 125 W kg^{-1}, whereas can still maintain 13.7 W h kg^{-1}, even at a power density of 3283 W kg^{-1}. As it can be observed in this figure, the values show a much improved energy density at high power density compared with a CNT//CNT symmetric device (6.1 W h kg^{-1} at 195 W kg^{-1}),[41] a $LiMn_2O_4//MnFe_2O_4$ asymmetric device (5.5 W h kg^{-1} at 1080 W kg^{-1}),[42] a $NiCo_2O_4–MnO_2//activated graphene asymmetric device (9.4 W h kg^{-1} at 175 W kg^{-1}),[43] a $Ni(OH)_2$–graphene//AC asymmetric device (11.11 W h kg^{-1} at 64 W kg^{-1}),[44] a TiO_2–CNT//CNT asymmetric device (4.47 W h kg^{-1} at 50 W kg^{-1}),[45] and a $CoMoO_4$–graphene//AC asymmetric device (3.59 W h kg^{-1} at 6000 W kg^{-1}).[46] Moreover, the $CuCo_2O_4@CuCo_2O_4//AC$ ASC device showed a high cycling stability of about 101.36% capacity retention after 2000 cycles even at a high current density of 30 mA cm^{-2} (Fig. 5f), indicating that it has great potential in practical applications as one of the most attractive candidates for energy storage.

4. Conclusion

In conclusion, we have facilely synthesized uniform hierarchical nanowire arrays $CuCo_2O_4@CuCo_2O_4$ supported on Ni foam by a two-step approach, which involves hydrothermal and calcination methods. The as-prepared product has been directly used as a binder- and additive-free electrode in the electrochemical investigation for supercapacitors. According to the obtained results, the $CuCo_2O_4@CuCo_2O_4$ NWAs exhibited a high specific capacitance of 888.9 F g^{-1} at a scan rate of 2 mA cm^{-2} (much higher than that of the $CuCo_2O_4$ NWAs synthesized via a similar method) and excellent cycle life with 101.77% capacitance retention at 50 mA cm^{-2} after 2000 cycles. Moreover, the as-fabricated ASC device based on the $CuCo_2O_4@CuCo_2O_4//AC$ hierarchical nanowires exhibited a maximum energy density of 18.0 W h kg^{-1}, which gradually decreased to 13.7 W h kg^{-1} as the power density increased from 125 W kg^{-1}

to 3283 W kg^{-1}. Our study reveals that this unique integrated nanostructure shall have great promise as superior electrochemical electrodes for the next generation electrochemical energy storage devices.

Acknowledgements

References

1 E. T. Mombeshora and V. O. Nyamori, *Int. J. Energy Res.*, 2015, **39**, 1955–1980.

2 J. B. Cheng, H. L. Yan, Y. Lu, K. W. Qiu, X. Y. Hou, J. Y. Xu, L. Han, X. M. Liu, J. K. Kim and Y. S. Luo, *J. Mater. Chem. A*, 2015, **3**, 9769–9776.

3 Q. Zhang, Y. H. Deng, Z. H. Hu, Y. F. Liu, M. M. Yao and P. P. Liu, *Phys. Chem. Chem. Phys.*, 2014, **16**, 23451–23460.

4 Y. Zhang, J. Xu, Y. Y. Zheng, X. Y. Hu, Y. Y. Shang and Y. J. Zhang, *RSC Adv.*, 2016, **6**, 59976–59983.

5 D. P. Cai, D. D. Wang, B. Liu, L. L. Wang, Y. Liu, H. Li, Y. R. Wang, Q. H. Li and T. H. Wang, *ACS Appl. Mater. Interfaces*, 2014, **6**, 5050–5055.

6 J. Xu, S. L. Gai, F. He, N. Niu, P. Gao, Y. J. Chen and P. P. Yang, *J. Mater. Chem. A*, 2014, **2**, 1022–1031.

7 L. Y. Lin, T. M. Liu, J. L. Liu, R. Sun, J. H. Hao, K. M. Ji and Z. C. Wang, *Appl. Surf. Sci.*, 2016, **360**, 234–239.

8 R. J. Zou, M. F. Yuen, Z. Y. Zhang, J. Q. Hu and W. J. Zhang, *J. Mater. Chem. A*, 2015, **3**, 1717–1723.

9 S. Abouali, M. A. Garakani, Z. L. Xu and J. K. Kim, *Carbon*, 2016, **102**, 262–272.

10 Q. F. Wang, D. Chen and D. H. Zhang, *RSC Adv.*, 2015, **5**, 96448–96454.

11 A. Shanmugavani and R. K. Selvan, *Electrochim. Acta*, 2015, **188**, 852–862.

12 W. M. Zhang, Z. W. Zhou, X. Y. Shan, R. Xu, Q. Chen, G. Y. He, X. Q. Sun and H. Q. Chen, *New J. Chem.*, 2016, **40**, 4769–4774.

13 J. L. Cheng, X. H. Li, Z. X. Wang, H. J. Guo, W. J. Peng and Q. Y. Hu, *Ceram. Int.*, 2016, **42**, 2871–2875.

14 Q. F. Wang, J. Xu, X. F. Wang, B. Liu, X. J. Hou, G. Yu, P. Wang, D. Chen and G. Z. Shen, *ChemElectroChem*, 2014, **1**, 559–564.

15 L. Q. Mai, F. Dong, X. Xu, Y. Z. Luo, Q. Y. An, Y. L. Zhao, J. Pan and J. N. Yang, *Nano Lett.*, 2013, **13**, 740–745.

16 F. X. Wang, Y. X. Zeng, D. Z. Zheng, C. Li, P. Liu, X. H. Lu and Y. X. Tong, *Carbon*, 2016, **103**, 56–62.

17 Y. B. He, Y. L. Bai, X. F. Yang, J. Y. Zhang, L. P. Kang, H. Xu, F. Shi, Z. B. Lei and Z. H. Liu, *J. Power Sources*, 2016, **317**, 10–18.

18 L. J. Zhang, K. N. Hui, K. S. Hui and H. Lee, *J. Power Sources*, 2016, **318**, 76–85.

19 Y. Zhang, J. Xu, Y. J. Zhang and X. Y. Hu, *J. Mater. Sci.: Mater. Electron.*, 2016, **27**, 1–7.

20 D. Z. Kong, C. W. Cheng, Y. Wang, J. I. Wong, Y. P. Yang and H. Y. Yang, *J. Mater. Chem. A*, 2015, **3**, 16150–16161.

21 X. Z. Wang, Y. H. Xiao, D. C. Su, L. M. Zhou, S. D. Wu, L. F. Han, S. M. Fang and S. K. Cao, *Electrochim. Acta*, 2016, **194**, 377–384.

22 W. J. Ren, D. Guo, M. Zhou, B. K. Guan, D. Zhang and Q. H. Li, *RSC Adv.*, 2015, **5**, 21881–21887.

23 X. Y. Liu, S. J. Shi, Q. Q. Xiong, L. Li, Y. J. Zhang, H. Tang, C. D. Gu, X. L. Wang and J. P. Tu, *ACS Appl. Mater. Interfaces*, 2013, **5**, 8790–8795.

24 H. C. Chen, S. Chen, H. Y. Shao, C. Li, M. Q. Fan, D. Chen, G. L. Tian and K. Y. Shu, *Chem.–Asian J.*, 2016, **11**, 248–255.

25 X. T. Zheng, Y. L. Ye, Q. Yang, B. Y. Geng and X. J. Zhang, *Dalton Trans.*, 2016, **45**, 572–578.

26 D. P. Cai, B. Liu, D. D. Wang, L. L. Wang, Y. Liu, H. Li, Y. R. Wang, Q. H. Li and T. H. Wang, *J. Mater. Chem. A*, 2014, **2**, 1954–1960.

27 T. Liu, H. Chai, D. Z. Jia, Y. Su, T. Wang and W. Y. Zhou, *Electrochim. Acta*, 2015, **180**, 998–1006.

28 X. C. Dong, H. Xu, X. W. Wang, Y. X. Huang, M. B. Chan-Park, H. Zhang, L. H. Wang, W. Huang and P. Chen, *ACS Nano*, 2012, **6**, 3206–3213.

29 C. Wu, J. J. Cai, Q. B. Zhang, X. Zhou, Y. Zhu, P. K. Shen and K. L. Zhang, *ACS Appl. Mater. Interfaces*, 2015, **7**, 26512–26521.

30 W. W. Zhou, D. Z. Kong, X. T. Jia, C. Y. Ding, C. W. Cheng and G. W. Wen, *J. Mater. Chem. A*, 2014, **2**, 6310–6315.

31 W. Zeng, G. H. Zhang, X. Wu, K. Zhang, H. Zhang, S. C. Hou, C. C. Li, T. H. Wang and H. G. Duan, *J. Mater. Chem. A*, 2015, **3**, 24033–24040.

32 G. L. Wang, J. C. Huang, S. L. Chen, Y. Y. Gao and D. X. Cao, *J. Power Sources*, 2011, **196**, 5756–5760.

33 W. B. Fu, Y. L. Wang, W. H. Han, Z. M. Zhang, H. M. Zha and E. Q. Xie, *J. Mater. Chem. A*, 2016, **4**, 173–182.

34 G. Jiang, M. Y. Zhang, X. Q. Li and H. Gao, *RSC Adv.*, 2015, **5**, 69365–69370.

35 X. D. Zhang, J. L. Xiao, X. Y. Zhang, Y. Meng and D. Xiao, *Electrochim. Acta*, 2016, **191**, 758–766.

36 W. Chen, C. Xia and N. H. Alshareef, *ACS Nano*, 2014, **8**, 9531–9541.

37 D. Cheng, Y. F. Yang, J. L. Xie, C. J. Fang, G. Q. Zhang and J. Xiong, *J. Mater. Chem. A*, 2015, **3**, 14348–14357.

38 C. C. Tu, L. Y. Lin, B. C. Xiao and Y. S. Chen, *J. Power Sources*, 2016, **320**, 78–85.

39 A. Pendashteh, J. Palma, M. Anderson and R. Marcilla, *J. Mater. Chem. A*, 2015, **3**, 16849–16859.

40 Z. X. Gu, R. F. Wang, H. H. Nan, B. Y. Geng and X. J. Zhang, *J. Mater. Chem. A*, 2015, **3**, 14578–14584.

41 B. Q. Wang, Z. H. Wen and J. H. Li, *Adv. Funct. Mater.*, 2006, **16**, 2141–2146.

42 Y. P. Lin and N. L. Wu, *J. Power Sources*, 2011, **196**, 851–854.

43 M. Kuang, Z. Q. Wen, X. L. Guo, S. M. Zhang and Y. X. Zhang, *J. Power Sources*, 2014, **270**, 426–433.

44 X. Wang, J. Y. Liu, Y. Y. Wang, C. M. Zhao and W. T. Zheng, *Mater. Res. Bull.*, 2014, **52**, 89–95.

45 X. Sun, M. Xie, J. J. Travis, G. K. Wang, H. T. Sun, J. Lian and S. M. George, *J. Phys. Chem. C*, 2013, **117**, 22497–22508.

46 X. Z. Yu, B. G. Lu and Z. Xu, *Adv. Mater.*, 2014, **26**, 1044–1051.